

Atomic and electronic structures of FeSe monolayer and bilayer thin films on SrTiO₃ (001): a first-principles study

Kai Liu¹, Zhong-Yi Lu¹, and Tao Xiang^{2,3}

¹*Department of Physics, Renmin University of China, Beijing 100872, China*

²*Institute of Theoretical Physics, Chinese Academy of Sciences, Beijing 100190, China and*

³*Institute of Physics, Chinese Academy of Sciences, Beijing 100190, China*

(Dated: October 30, 2018)

By the first-principles electronic structure calculations, we have studied electronic structures of FeSe monolayer and bilayer thin films on SrTiO₃ (001) with SrO termination or TiO₂ termination. We find that both FeSe monolayer and bilayer on either termination behave like a slightly doped semiconductor and a collinear antiferromagnetic order on Fe ions. There is no substantial charge transfer between the FeSe layers and the substrate. FeSe is adhered to the SrTiO₃ surface by a dipole-dipole interaction. The Fermi surface is mainly the contribution of Fe-3*d* orbitals. A valence band contributed mainly by the O-2*p* orbitals in the TiO₂ layer is located slightly below the Fermi level, which can become conducting upon a small doping of holes.

PACS numbers: 68.35.B-, 73.20.-r, 74.70.Dd, 68.43.Bc

I. INTRODUCTION

The discovery of Fe-based superconductors¹⁻⁴ has inspired worldwide interests both experimentally and theoretically in the recent years. The common feature of all the Fe-based superconductor compounds is that they have FeX layers (X=P, As, S, Se or Te) composed of edge-sharing tetrahedra with an Fe center. Furthermore, some of the parent compounds of these superconductors are antiferromagnetic (AFM) semimetals⁵ with either a collinear^{6,7} or bi-collinear^{8,9} AFM order below a structural transition temperature. The superconductivity can be induced either by hole or electron doping via chemical substitution or by high pressure, and the superconducting paring is believed to occur in the FeX layers.

In Fe-based superconductors, it was widely believed that the As-bridged antiferromagnetic superexchange interaction between the next nearest neighbors Fe-Fe atoms plays an important role^{7,10}. This kind of interaction depends strongly on the local geometry of a Fe-As bond. Indeed, it was found that the geometry of the FeX₄ tetrahedral unit, in particular the bond length and the bond angle between two neighboring X and Fe ions, strongly correlates with the superconductivity transition temperature^{11,12}. Besides applying pressure, growing an Fe-based superconductor on some substrate is another effective way to manipulate the lattice parameters and the FeX₄ tetrahedral geometry, which may tune the superconducting transition temperature. As an orthodox metal oxide perovskite, Strontium titanate (SrTiO₃) is widely used as a high-quality substrate for epitaxial growth of high-temperature cuprate superconductors and many other oxide-based thin films¹³. Very recently, SrTiO₃ has been used as a substrate to epitaxially grow FeSe ultrathin films¹⁴. It is found that the monolayer FeSe thin film grown on SrTiO₃ (001) shows signatures of superconducting transition above 50 K by transport measurement, while the bilayer and thicker films, in contrast, do not show any sign of superconductivity¹⁴.

To understand the physics underlying this remarkable finding, we have performed the first-principles electronic structure calculations on FeSe monolayer and bilayer ultrathin films on SrTiO₃ (001), respectively. We find that both monolayer and bilayer thin films show a semiconducting behavior with a collinear AFM order on Fe atoms, substantially different from the metallic bulk FeSe. Considering the difference between the single FeSe and multi-layer FeSe thin films, this suggests that the observed superconductivity happens either at the interface of FeSe-SrTiO₃ or just in the first FeSe layer, not in the other FeSe layers.

Crystal SrTiO₃ is built from alternatively stacking planar SrO and TiO₂ square layers along the *c*-axis. Experimentally, bulk SrTiO₃ takes a structural phase transition from cubic perovskite structure into a tetragonal one at 105K, in which each octahedral unit TiO₆ with titanium centered slightly rotates around the *z* axis, meanwhile the rotation directions between the nearest neighboring octahedral units are reverse with each other^{15,16}. Such a structural distortion is thus called antiferrodistortion.

The cleaving of SrTiO₃ simultaneously generates both SrO-terminated and TiO₂-terminated surfaces with the corresponding cleavage energy equally distributed between these two surfaces^{17,18}. It was further shown that the surface energies are nearly the same for these two surfaces after full relaxation^{18,19}. This means that both surfaces are stable and either of them may be used as a substrate to grow FeSe thin films. We thus study FeSe monolayer and bilayer on both TiO₂-terminated and SrO-terminated SrTiO₃ (001), respectively.

II. COMPUTATIONAL DETAILS

To study the atomic structures and the electronic and magnetic properties of FeSe ultrathin films on SrTiO₃ (001), we carried out the fully spin-polarized first-principles electronic structure calculations by us-

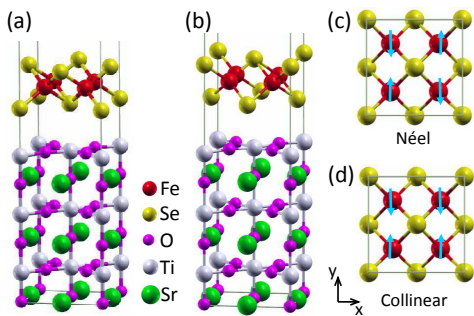


FIG. 1: (Color online) Atomic structures (a)I and (b)II of monolayer FeSe on TiO_2 -terminated $\text{SrTiO}_3(001)$ surface. Patterns of Fe atom spins in the (c)checkerboard antiferromagnetic Néel state and (d)the collinear antiferromagnetic state.

ing the projector augmented wave (PAW) method^{20,21}. We adopted the generalized gradient approximation of Perdew-Burke-Ernzerhof²² for the exchange-correlation potentials. After the full convergence test, the kinetic energy cut-off of the plane wave basis was chosen to be 400 eV. The optimization made the forces on all relaxed atoms smaller than 0.02 eV/Å.

We first checked the properties of bulk SrTiO_3 . We constructed a 20-atom tetragonal supercell so that we can describe the antiferrodistortive structure, which unit cell is $\sqrt{2} \times \sqrt{2} \times 2$ unit cell of undistortive bulk SrTiO_3 . The Brillouin zone was sampled with a $6 \times 6 \times 6$ \mathbf{k} -point mesh. After both the shape and volume of the supercell and the internal atomic positions were optimized, we find that SrTiO_3 has indeed an antiferrodistortive tetragonal structure with the lattice parameters $a^* = b^* = \sqrt{2}a = 5.536$ Å and $c^* = 2c = 7.831$ Å (a and c being the lattice parameters of the undistortive tetragonal unit cell), the octahedral rotation angle $\theta = 1.1^\circ$, and the ratio $(c/a) - 1 = 3 \times 10^{-4}$. These values agree well with the experimental data¹⁶ $a^* = b^* = 5.507$ Å, $c^* = 7.796$ Å, $\theta = 2.1^\circ$, and $(c/a) - 1 = 10 \times 10^{-4}$, respectively, as well as with the previous calculation results²³.

To model FeSe ultrathin films on TiO_2 (SrO)- terminated $\text{SrTiO}_3(001)$, we used a 6 (7)-layer $\text{SrTiO}_3(001)$ slab with FeSe monolayer and bilayer FeSe adsorbed on the top side in a $\sqrt{2}a \times \sqrt{2}a$ two-dimensional supercell plus a vacuum layer of about 10 Å. The top two slab layers and all FeSe layer atoms were allowed to relax while the rest slab layers were fixed at their bulk positions. A $6 \times 6 \times 1$ \mathbf{k} -point mesh for the Brillouin zone sampling and the Gaussian smearing technique with a width of 0.1 eV were used. The electric field induced by asymmetric slab relaxation was compensated by a dipole correction²⁴.

III. RESULTS AND ANALYSIS

For both TiO_2 -terminated and SrO-terminated SrTiO_3 substrates, we studied two possible adsorption structures of FeSe thin films as shown in Fig. 1 (a) and (b) and

Fig. 2 (a) and (b), respectively. The nonmagnetic, the ferromagnetic, the checkerboard antiferromagnetic Néel, and the collinear antiferromagnetic states were all calculated. Patterns of Fe atom spins in the checkerboard antiferromagnetic Néel and the collinear antiferromagnetic states are shown in panels (c) and (d) of Fig. 1 and Fig. 2, respectively. To better understand the electronic properties of FeSe thin films on SrTiO_3 , the electronic band structures of clean SrTiO_3 surface and isolated FeSe monolayer are firstly introduced in subsection A. Results of monolayer and bilayer FeSe ultrathin films on TiO_2 -terminated and SrO-terminated SrTiO_3 are then presented in subsection B and C, respectively.

Figure 1 shows the atomic structures of monolayer FeSe on TiO_2 -terminated SrTiO_3 surface. For structure I in panel (a), Se atom locates on top of the Ti atom, which substitutes the position of O atom in TiO_6 octahedron of bulk SrTiO_3 . For structure II in panel (b), Se atom sits on the center site of the Ti-Ti square. The atomic structures of monolayer FeSe on SrO-terminated SrTiO_3 surface are shown in Fig. 2. For structure I in panel (a), Se atom locates on top of the O atom. As to the structure II in panel (b), Se atom is on top of the Sr atom. By considering the symmetry of both the ad-layer and the substrate, these four structures in Figs. 1 and 2 are the most possible adsorption sites.

A. Clean SrTiO_3 surface and isolated FeSe monolayer

In order to have a concept about how the electronic structures of FeSe- SrTiO_3 heterostructures are derived from their subdivisions, we firstly studied the band structures of TiO_2 - and SrO-terminated $\text{SrTiO}_3(001)$ clean surfaces and isolated FeSe monolayer. For SrO-terminated surface, the atomic structure of a 7-layer slab is the same as the substrate of $\sqrt{2}a \times \sqrt{2}a$ two-dimensional supercell in Fig. 2. For TiO_2 -terminated case, the TiO_2 and SrO layers exchange their vertical positions. Regarding the isolated FeSe monolayer, its in-

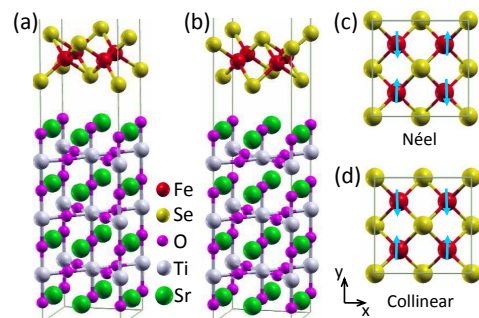


FIG. 2: (Color online) Atomic structures (a)I and (b)II of monolayer FeSe on SrO-terminated $\text{SrTiO}_3(001)$ surface. Patterns of Fe atom spins in the (c)checkerboard antiferromagnetic Néel state and (d)the collinear antiferromagnetic state.

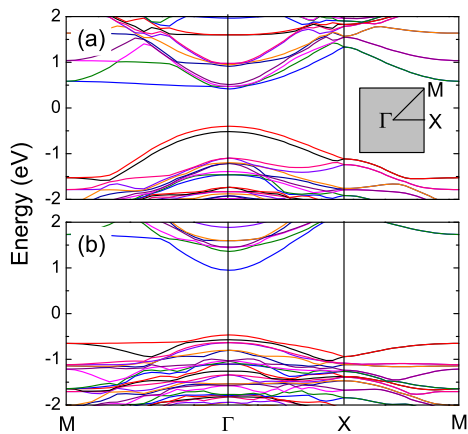


FIG. 3: (Color online) Band structures of clean (a)TiO₂-terminated and (b)SrO-terminated SrTiO₃(001) surface along high symmetric directions of surface Brillouin zone (SBZ) in the inset.

plane lattice constants were fixed at the value of SrTiO₃ surface as in Fig. 1. This corresponds to 3.91 Å for the in-plane distance of Se-Se atom. We also checked the case of 3.8 Å as reported in the experiment¹⁴. There is no meaningful change found.

Figure 3 shows the band structures of clean TiO₂- and SrO-terminated SrTiO₃ surface in panel (a) and (b), respectively. The surface Brillouin zone (SBZ) of the $\sqrt{2}a \times \sqrt{2}a$ two-dimensional supercell is shown as the inset of panel (a). In the following of the paper, we always use the same SBZ since all structures studied have the same two-dimensional supercell. As can be seen from panel (a) for TiO₂-terminated surface, there are two nearly degenerated valence bands separated from the conduction bands by a gap of about 1 eV. These two valence bands are derived from the 2*p* orbitals of O atoms in the surface TiO₂ layers of the two-sided slab. The bottom of the conduction band is contributed by the 3*d* orbitals of Ti atoms in the deep layers. As a contrast, for SrO-terminated surface in panel (b), the top valence band is formed by the 2*p* orbitals of O atoms in the deep layers while the bottom conduction band originates from the 3*d* orbitals of subsurface Ti atoms. The band gaps of clean SrTiO₃ surface are thus determined by the orbitals of O and Ti atoms for both terminations. These results are consistent with the previous calculations^{18,19}.

The band structures of isolated FeSe monolayer with lattice parameter of 3.91 Å in the nonmagnetic and collinear antiferromagnetic states are shown in Fig. 4 (a) and (b), respectively. As we see, there are two electron-type bands and two hole-type bands around Γ point in the nonmagnetic state, which is due to the band folding effect since here the unit cell is $\sqrt{2} \times \sqrt{2}$ unit cell of bulk FeSe on *ab*-plane. In the collinear antiferromagnetic state, an obvious feature is the Dirac-Cone-like bands at Γ point along $M-\Gamma-X$ with the Fermi level slightly below the Dirac point and the tiny density of states at the Fermi level. The isolated FeSe monolayer in the collinear

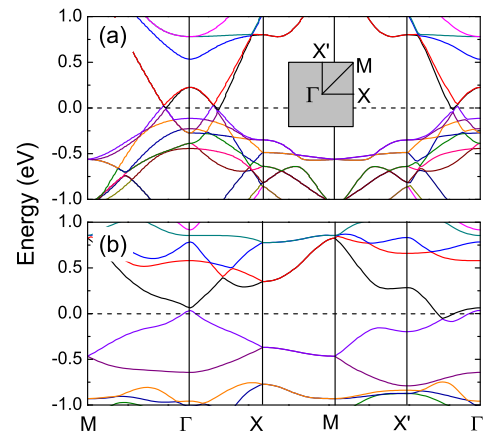


FIG. 4: (Color online) Band structures of isolated FeSe monolayer along high symmetric directions of SBZ: (a) nonmagnetic state; (b) collinear antiferromagnetic state, in which ΓX corresponds to the spins in parallel and $\Gamma X'$ to the spins in anti-parallel. The Fermi energy is set to zero.

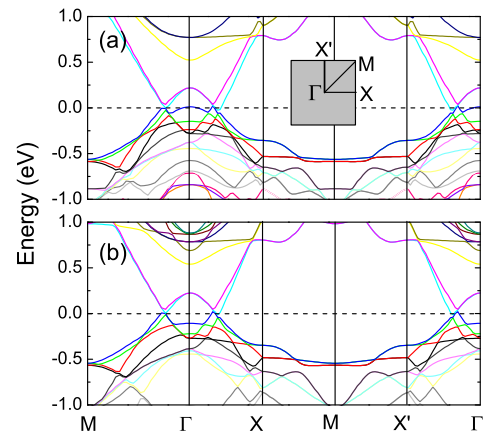


FIG. 5: (Color online) Band structures of (a)structure I and (b)structure II for monolayer FeSe on TiO₂-terminated SrTiO₃ in nonmagnetic state along high symmetric directions of SBZ shown in panel (a). The Fermi energy is set to zero.

antiferromagnetic state thus shows a semiconducting behavior.

B. FeSe on TiO₂-terminated SrTiO₃

1. Monolayer FeSe

For monolayer FeSe on TiO₂-terminated SrTiO₃, the substrate is simulated with a 6-layer slab as shown in Fig. 1, which eliminates one of the two nearly degenerated top valence bands shown in Fig. 3(a).

The band structures of structure I and II (Fig. 1) for the monolayer FeSe on TiO₂-terminated SrTiO₃ in the nonmagnetic state along high symmetric directions of SBZ are shown in panels (a) and (b) of Fig. 5, respectively. For both structures, there are two electron-type

bands and two hole-type bands around Γ point, similar to the case of the isolated monolayer FeSe, which is clearly due to the band folding effect. The main difference between (a) and (b) is the relative position of the band at Γ point just below the Fermi level (blue line in panel (a) and yellow line in panel (b)). This band touches the Fermi level at Γ point for structure I while it falls below the Fermi level for structure II, which corresponds to the valence band of the substrate.

By comparing the energies of the nonmagnetic state, ferromagnetic state, checkerboard antiferromagnetic Néel state, and collinear antiferromagnetic state, we find that the ground state is the collinear antiferromagnetic state with a large magnetic moment of $2.5 \mu_B$ on each Fe atom for both structures I and II. In the ground state, the vertical distances of Se atom to the TiO_2 plane are 3.06 \AA and 3.16 \AA in structure I and II, respectively. The total energy of structure I is lower by 0.2 eV than that of structure II. These indicate that the FeSe monolayer has a stronger bonding with the substrate in structure I than in structure II.

Figure 6 shows the band structures of structure I and II for the monolayer FeSe on TiO_2 -terminated SrTiO_3 in the collinear antiferromagnetic state. Compared with Fig. 3(a) and Fig. 4(b), the bands of structure I in Fig. 6(a) seems to be a superposition of the bands of separated substrate and FeSe monolayer. The Fermi level is pinned on the top of valence band of TiO_2 -terminated SrTiO_3 , i.e. Dirac-Cone-like bands of FeSe lining up the Fermi level with the parabolic valence band of the substrate. However, such a parabolic band shifts downwards away from the Fermi level for the structure II in panel (b).

In order to clarify the contributions to the bands near Fermi level from different orbitals, we plot the orbital-resolved partial density of states for structures I and II of the monolayer FeSe on TiO_2 -terminated SrTiO_3 in the

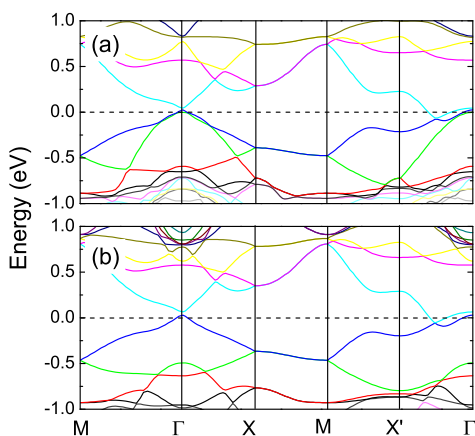


FIG. 6: (Color online) Band structures of (a) structure I and (b) structure II for monolayer FeSe on TiO_2 -terminated SrTiO_3 in collinear antiferromagnetic state along high symmetric directions of SBZ, in which ΓX corresponds to the spins in parallel and $\Gamma X'$ to the spins in anti-parallel. The Fermi energy is set to zero.

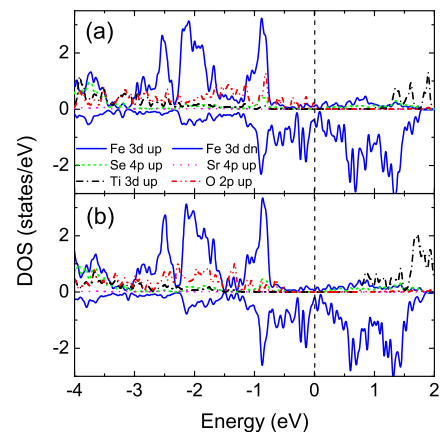


FIG. 7: (Color online) Orbital-resolved partial density of states of (a) structure I and (b) structure II for monolayer FeSe on TiO_2 -terminated SrTiO_3 in collinear antiferromagnetic state. The Fermi energy is set to zero.

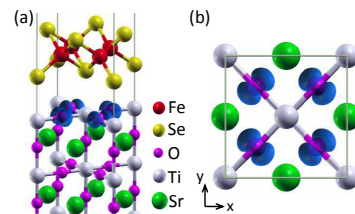


FIG. 8: (Color online) Side view (a) and top view (b) of band decomposed charge density isosurface ($0.001 \text{ e}/\text{\AA}^3$) of monolayer FeSe on TiO_2 -terminated SrTiO_3 in collinear antiferromagnetic state for the parabolic valence band around Γ point in Fig. 6(a).

collinear antiferromagnetic state in panels (a) and (b) of Fig. 7, respectively. In both panels, the Fe atom $3d$ orbitals contribute to the density of state around the Fermi level, which is located at a valley. The main difference between panels (a) and (b) is that the $2p$ orbitals of surface O atoms (red dash dot dot line) in TiO_2 -terminated SrTiO_3 show states near the Fermi level for structure I, while they are absent for structure II. This indicates that the parabolic valence band just below the Fermi level in Fig. 6 belongs to surface O atoms, which is further confirmed by the band decomposed charge density shown in Fig. 8. As can be seen from the side and top views in Fig. 8, this parabolic valence band originates from the p_x and p_y orbitals of surface O atoms in the TiO_2 termination layer.

2. Bilayer FeSe

For bilayer FeSe on TiO_2 -terminated SrTiO_3 , the possible positions of first layer of FeSe are structure I and II in Fig. 1 while the second layer of FeSe arranges according to their bulk positions. We still refer them to structure I and II in the following.

Figure 9 shows the band structures of structure I and II for bilayer FeSe on TiO_2 -terminated SrTiO_3 in the collinear antiferromagnetic state. Compared with the band structures of the monolayer FeSe on TiO_2 -terminated SrTiO_3 in Fig. 6, the number of bands near the Fermi level contributed by the Fe atoms is doubled. This feature is similar to the band structure of bilayer graphene near K point. Moreover, the parabolic valence band near Γ point in panel (a), which originates from the surface O atoms, shows little shift compared with its corresponding band in Fig. 6.

The orbital-resolved partial density of states for structure I and II of the bilayer FeSe on TiO_2 -terminated SrTiO_3 in the collinear antiferromagnetic state are shown in panels (a) and (b) of Fig. 10, respectively. Similar to the monolayer case, the Fe atoms contribute to the density of state around the Fermi level, and the surface O atoms of structure I in TiO_2 -terminated SrTiO_3 show states near the Fermi level, which are due to the parabolic valence band near Γ point in Fig. 9.

C. FeSe on SrO-terminated SrTiO_3

1. Monolayer FeSe

The band structures of structure I and II for the monolayer FeSe on SrO-terminated SrTiO_3 in the nonmagnetic state along high symmetric directions of SBZ are shown in panels (a) and (b) of Fig. 11, respectively. For both structures, there are two electron-type bands and two hole-type bands around Γ point of the SBZ. The parabolic valence band just below the Fermi level comes from the valence band of the substrate, the other bands crossing the Fermi level again due to the band folding effect.

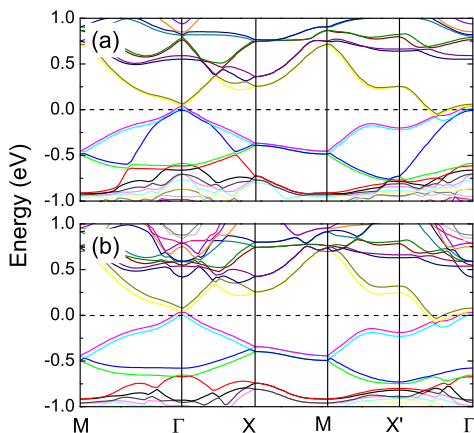


FIG. 9: (Color online) Band structures of (a)structure I and (b)structure II for bilayer FeSe on TiO_2 -terminated SrTiO_3 in collinear antiferromagnetic state along high symmetric directions of SBZ, in which ΓX corresponds to the spins in parallel and $\Gamma X'$ to the spins in anti-parallel. The Fermi energy is set to zero.

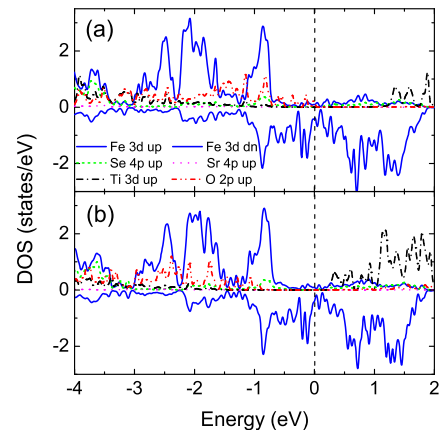


FIG. 10: (Color online) Orbital-resolved partial Density of states of (a)structure I and (b)structure II for bilayer FeSe on TiO_2 -terminated SrTiO_3 in collinear antiferromagnetic state. The Fermi energy is set to zero.

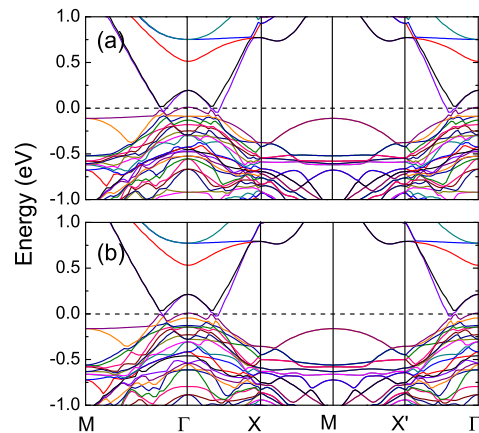


FIG. 11: (Color online) Band structures of (a)structure I and (b)structure II for monolayer FeSe on SrO-terminated SrTiO_3 in nonmagnetic state along high symmetric directions of SBZ. The Fermi energy is set to zero.

By comparing the energies of the nonmagnetic state, ferromagnetic state, checkerboard antiferromagnetic Néel state, and collinear antiferromagnetic state, we find that the ground state of monolayer FeSe on SrO-terminated SrTiO_3 is also the collinear antiferromagnetic state with a large magnetic moment, similar to the case of TiO_2 termination. In this state, the vertical distances of Se atom to the TiO_2 plane are 3.67 \AA and 3.64 \AA in structure I and II, respectively. The total energy of structure II is slightly lower by 0.06 eV than that of structure I.

Figure 12 shows the band structures of structure I and II for the monolayer FeSe on SrO-terminated SrTiO_3 in the collinear antiferromagnetic state. The bands near the Fermi level look like the superposition of the bands of the substrate in Fig. 3(b) and the isolated FeSe monolayer in Fig. 4(b), similar to the case of TiO_2 -termination. However, there is obvious difference between the bands shown in Fig. 12 and 6. This may origin from the different char-

acteristics of SrO-terminated and TiO₂-terminated surfaces, for which Ti-O bond shows considerable covalency near the surface^{18,19}.

The orbital-resolved partial density of states for structure I and II of the monolayer FeSe on SrO-terminated SrTiO₃ in the collinear antiferromagnetic state are shown in panels (a) and (b) of Fig. 13, respectively. The O-s denotes surface O atom in SrO termination layer and the O-c is O atom in the TiO₂ deep layers. In both panels, the Fe atoms contribute most to the density of state around the Fermi level, which is located at a valley. However, the O atoms in the TiO₂ deep layers contribute more to the states near Fermi level than the surface O atoms in the SrO termination. This is consistent with the previous calculations that the upper valence band for the SrO-terminated surface is mainly formed from the orbitals of internal O atoms^{18,19}.

In order to illustrate the origin of the parabolic valence band near the Fermi level along $M - \Gamma - X$ direction in Fig. 12, the band decomposed charge density is plotted in Fig. 14. As can be seen from the side view and top view, this parabolic band originates from the $2p$ orbitals of O atoms in the TiO₂ deep layers. This is in agreement with the density of states in Fig. 13.

2. Bilayer FeSe

Similar to the case of TiO₂ termination, for bilayer FeSe on SrO-terminated SrTiO₃, the possible positions of first layer of FeSe are structure I and II in panels (a) and (b) of Fig. 2, respectively. The second layer of FeSe arranges according to their bulk positions.

Figure 15 shows the band structures of structure I and II for the bilayer FeSe on SrO-terminated SrTiO₃ in the collinear antiferromagnetic state. As can be seen near

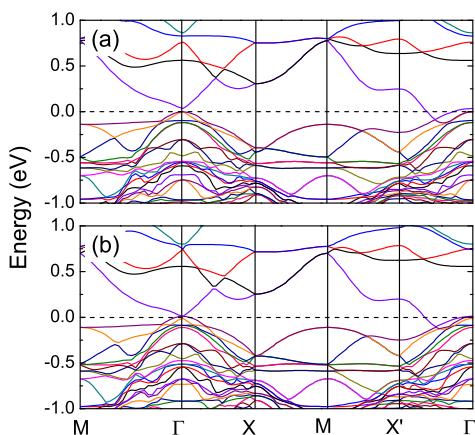


FIG. 12: (Color online) Band structures of (a)structure I and (b)structure II for monolayer FeSe on SrO-terminated SrTiO₃ in collinear antiferromagnetic state along high symmetric directions of SBZ, in which ΓX corresponds to the spins in parallel and $\Gamma X'$ to the spins in anti-parallel. The Fermi energy is set to zero.

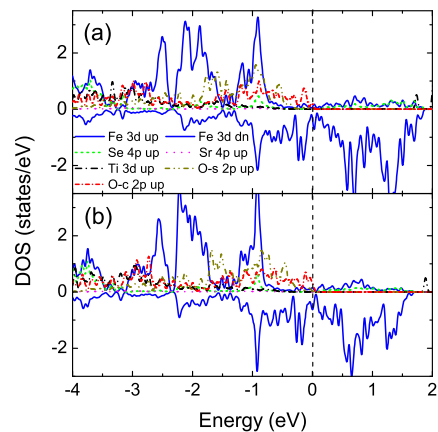


FIG. 13: (Color online) Orbital-resolved partial density of states of (a)structure I and (b)structure II for monolayer FeSe on SrO-terminated SrTiO₃ in collinear antiferromagnetic state. The O-s denotes surface O atom in SrO termination layer and the O-c is O atom in the TiO₂ deep layer. The Fermi energy is set to zero.

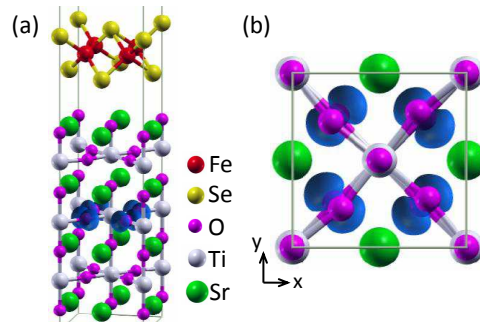


FIG. 14: (Color online) Side view (a) and top view (b) of band decomposed charge density isosurface ($0.001 e/\text{\AA}^3$) of monolayer FeSe on SrO-terminated SrTiO₃ in collinear antiferromagnetic state for the parabolic valence band near Γ point in Fig. 12.

the Fermi level, the number of bands contributed by the Fe atoms is doubled as well. The parabolic valence band near Γ point in panel (a), which originates from O atoms in the TiO₂ deep layers, shows slight shift compared with its corresponding band in Fig. 12.

Figure 16 shows the orbital-resolved partial density of states for structure I and II of the bilayer FeSe on SrO-terminated SrTiO₃ in the collinear antiferromagnetic state. Similar to the previous results, the Fe atoms contribute to the density of state around the Fermi level responsible for the Dirac-Cone-like bands along $M - \Gamma - X$ direction in Fig. 15. The $2p$ orbitals of O atoms in the TiO₂ deep layers also show larger density of states near the Fermi level than the surface O atoms. Structures I and II have similar peaks in all energy ranges.

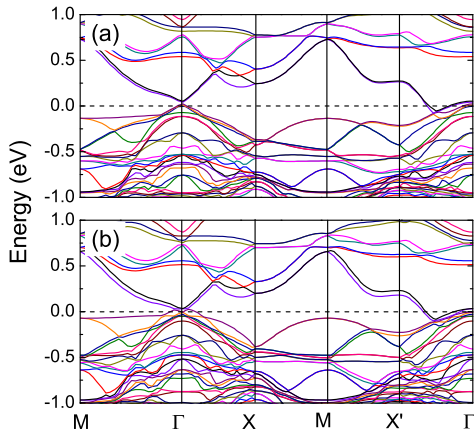


FIG. 15: (Color online) Band structures of (a) structure I and (b) structure II for bilayer FeSe on SrO-terminated SrTiO₃ in collinear antiferromagnetic state along high symmetric directions of SBZ, in which ΓX corresponds to the spins in parallel and $\Gamma X'$ to the spins in anti-parallel. The Fermi energy is set to zero.

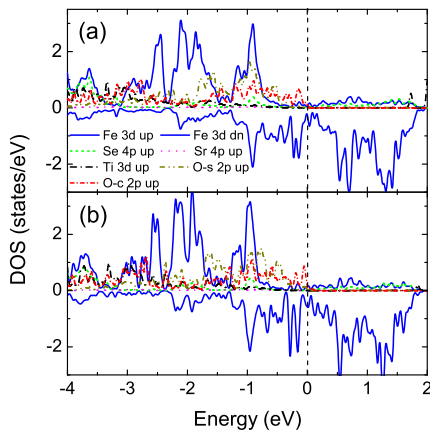


FIG. 16: (Color online) Orbital-resolved partial density of states of (a) structure I and (b) structure II for monolayer FeSe on SrO-terminated SrTiO₃ in collinear antiferromagnetic state. The Fermi energy is set to zero.

IV. DISCUSSION AND SUMMARY

Inspection of the orbital and layer resolved density of states in the calculations show that there is no substantial

charge transfer between FeSe layers and the substrate, as expected since both FeSe layer and SrTiO₃ layers are already balanced on the chemical valences. Thus there is no strong chemical bonding between the FeSe layer and the substrate SrTiO₃. This implies that the electronic band structure of FeSe ultrathin films on SrTiO₃ would result from the band lineup at the interface between the FeSe thin film and substrate SrTiO₃. The calculations indeed confirm this picture, as shown in Figs. 3, 4, 6, 9, 12, and 15. The Fermi level of FeSe thin films is found to locate at the top of the valence band of substrate SrTiO₃. The top valence band of TiO₂-terminated substrate mainly consists of O-2*p* orbitals within TiO₂ surface layer while O-2*p* orbitals within deep TiO₂ layers for SrO-terminated substrate. This band can become conducting by a small amount of hole-doping or by applying a small positive gate voltage. In the experiment of FeSe-SrTiO₃ heterostructure reported in Ref. 14, the superconductivity was found in the FeSe monolayer absorbed onto the TiO₂-terminated substrate, but not in the bilayer films. Our calculations show that the electronic band structures of FeSe monolayer and bilayer on TiO₂-termination have similar band structures. Both show a semiconducting behavior. This may suggest that the observed superconductivity happens either just in the interface of FeSe-SrTiO₃ heterostructures or in the first layer of FeSe, and the superconducting gap could not be observed in the double FeSe thin films by the experimental measurements because the tunneling current was blocked by the second FeSe layer.

Acknowledgments

We wish to thank Qikun Xue and Dunghai Lee for useful discussions. This work is supported by National Natural Science Foundation of China (Grant Nos. 11004243 and 11190024), National Program for Basic Research of MOST of China (Grant No. 2011CBA00112), the Fundamental Research Funds for the Central Universities, and the Research Funds of Renmin University of China (08XNF018, 10XNL016). Computational resources have been provided by the Physical Laboratory of High Performance Computing at Renmin University of China. The atomic structures were prepared with the XCRYSDEN program²⁵.

¹ Y. Kamihara, T. Watanabe, M. Hirano, and H. Hosono, *J. Am. Chem. Soc.* **130**, 3296 (2008).

² M. Rotter, M. Tegel, and D. Johrendt, *Phys. Rev. Lett.* **101**, 107006 (2008).

³ X. C. Wang, Q. Q. Liu, Y. X. Lv, W. B. Gao, L. X. Yang, R. C. Yu, F. Y. Li, and C. Q. Jin, *Solid State Commun.* **148**, 538 (2008).

⁴ F.-C. Hsu, J.-Y. Luo, K.-W. Yeh, T.-K. Chen, T.-W. Huang, P. M. Wu, Y.-C. Lee, Y.-L. Huang, Y.-Y. Chu,

D.-C. Yan, and M.-K. Wu, *Proc. Natl. Acad. Sci. U.S.A.* **105**, 14262 (2008).

⁵ F. Ma and Z.-Y. Lu, *Phys. Rev. B* **78**, 033111 (2008).

⁶ C. de la Cruz, Q. Huang, J. W. Lynn, J. Li, W. Ratcliff II, J. L. Zarestky, H. A. Mook, G.F. Chen, J. L. Luo, N. L. Wang, and P. Dai, *Nature* **453**, 899 (2008).

⁷ F. Ma, Z.-Y. Lu, and T. Xiang, *Phys. Rev. B* **78**, 224517 (2008).

⁸ F. Ma, W. Ji, J. P. Hu, Z.-Y. Lu, and T. Xiang, *Phys. Rev.*

- Lett. **102**, 177003 (2009).
- ⁹ W. Bao, Y. Qiu, Q. Huang, M. A. Green, P. Zajdel, M. R. Fitzsimmons, M. Zhernenkov, S. Chang, M. Fang, B. Qian, E. K. Vehstedt, J. Yang, H. M. Pham, L. Spinu, and Z. Q. Mao, Phys. Rev. Lett. **102**, 247001 (2009).
- ¹⁰ K. Seo, A. B. Bernevig, J. Hu, Phys. Rev. Lett. **101**, 206404 (2008).
- ¹¹ C. H. Lee, A. Iyo, H. Eisaki, H. Kito, M. T. Fernandez-Diaz, T. Ito, K. Kihou, H. Matsuhata, M. Braden, and K. Yamada, J. Phys. Soc. Jpn. **77**, 083704 (2008).
- ¹² T. M. McQueen, M. Regulacio, A.J. Williams, Q. Huang, J. W. Lynn, Y. S. Hor, D. V. West, M. A. Green, and R. J. Cava, Phys. Rev. B **78**, 024521 (2008).
- ¹³ K. Ueno, S. Nakamura, H. Shimotani, A. Ohtomo, N. Kimura, T. Nojima, H. Aoki, Y. Iwasa, and M. Kawasaki, Nature Mater. **7**, 855 (2008).
- ¹⁴ Q.-Y. Wang, Z. Li, W.-H. Zhang, Z.-C. Zhang, J.-S. Zhang, W. Li, H. Ding, Y.-B. Ou, P. Deng, K. Chang, J. Wen, C.-L. Song, K. He, J.-F. Jia, S.-H. Ji, Y. Wang, L. Wang, X. Chen, X. Ma, and Q.-K. Xue, arXiv:1201.5694.
- ¹⁵ H. Unoki and T. Sakudo, J. Phys. Soc. Jpn. **23**, 546 (1967).
- ¹⁶ W. Jauch and A. Palmer, Phys. Rev. B **60**, 2961 (1999).
- ¹⁷ N. Bickel, G. Schmidt, K. Heinz, and K. Müller, Phys. Rev. Lett. **62**, 2009 (1989).
- ¹⁸ E. Heifets, R. I. Eglitis, E. A. Kotomin, J. Maier, and G. Borstel, Phys. Rev. B **64**, 235417 (2001).
- ¹⁹ E. Heifets, R. I. Eglitis, E. A. Kotomin, J. Maier, and G. Borstel, Surf. Sci. **513**, 211 (2002).
- ²⁰ G. Kresse, J. Hafner, Phys. Rev. B **47**, 558 (1993); G. Kresse, J. Furthmüller, Comp. Mater. Sci. **6**, 15 (1996); G. Kresse, J. Furthmüller, Phys. Rev. B **54**, 11169 (1996).
- ²¹ P. E. Blöchl, Phys. Rev. B **50**, 17953 (1994); G. Kresse, D. Joubert, Phys. Rev. B **59**, 1758 (1999).
- ²² J. P. Perdew, K. Burke, M. Ernzerhof, Phys. Rev. Lett. **77**, 3865 (1996).
- ²³ F. El-Mellouhi, E. N. Brothers, M. J. Lucero, and G. E. Scuseria, Phys. Rev. B **84**, 115122 (2011).
- ²⁴ J. Neugebauer and M. Scheffler, Phys. Rev. B **46**, 16067 (1992).
- ²⁵ A. Kokalj, Comp. Mater. Sci. **28**, 155 (2003). Code available from <http://www.xcrysden.org/>.